Experimental Investigation on Receptivity of Crossflow Instability to Discrete Roughness Amplitude and Location

Zoppini, G.; Ragni, D.; Kotsonis, M.

DOI
10.2514/6.2021-0152

Publication date
2021

Document Version
Final published version

Published in
AIAA Scitech 2021 Forum

AIAA SciTech Forum
11–15 & 19–21 January 2021, VIRTUAL EVENT
AIAA Scitech 2021 Forum

10.2514/6.2021-0152

Experimental Investigation on Receptivity of Crossflow Instability to Discrete Roughness Amplitude and Location

G. Zoppini *, D. Ragni † and M. Kotsonis ‡
Delft University of Technology, Delft, The Netherlands, 2629HS

An experimental parametric study of the effect of discrete roughness elements (DRE) on the development and breakdown of stationary crossflow instability on a swept wing is presented. A systematic investigation of the receptivity to various elements height and chord locations is carried out in a crossflow dominated flow. The flow is globally and locally investigated through simultaneous infra-red (IR) and planar particle image velocimetry (PIV) acquisitions that correlate the extracted transition location and the developing flow feature with the applied forcing configuration, providing insights on the physical mechanisms governing receptivity. The presented results show how a downstream shift in the DRE array location is accompanied by a transition delay, while an increase of the elements height leads to a transition advancement. Moreover, the entire set of PIV measurements allows to compare the instabilities development between different forcing cases, providing insights on the dominant physical mechanisms governing receptivity of stationary CFI to discrete roughness and possible scaling rules. In fact, an up-scaled forcing configuration replicating the instabilities strength and evolution would allow to investigate the near-flow features in a set-up easier to measure experimentally.

Nomenclature

α	=	Angle of attack, deg.	AR	=	Wing aspect ratio.
b	=	Wing span dimension, m.	C_p	=	Pressure coefficient.
c	=	Leading edge orthogonal chord, m.	c_X	=	Streamwise chord, m.
δ^*	=	Boundary-layer displacement thickness, mm.	D	=	DRE diameter, mm.
f	=	Lens focal length, mm.	$f\#$	=	Lens aperture.
k	=	DRE height, mm.	Λ	=	Sweep angle, deg.
λ_T	=	Wing taper ratio.	λ_z	=	Modes wavelength, mm.
N	=	N-factor.	R_q	=	RMS surface roughness, μm.
Re_k	=	Roughness Reynolds number, $\frac{\lvert\mathbf{u}(k)\rvert k}{\nu}$.	Re_{c_X}	=	Reynolds number, $\frac{U_\infty c_X}{\nu}$.
s	=	Stream-wise surface coordinate, m.	S	=	Wing planform area, m^2.
x_{TR}	=	Transition location.	x_{DRE}	=	DRE location.
W_∞	=	Span-wise free-stream velocity, ms^{-1}.	A	=	Instability amplitude.
$\overline{w}$	=	Time averaged span-wise velocity.	$\langle\overline{w}\rangle_z$	=	Disturbance velocity profiles.

I. Introduction

Swept-wings boundary layer stability and transition has been one of the major research topics in the last century, strongly motivated by the desire of improving Laminar Flow Control (LFC) techniques. In fact, in a modern transport aircraft about half of the total drag is caused by turbulent skin friction [1], therefore delaying transition to turbulence can enhance the wing aerodynamics and efficiency. In turn, this would lead to a reduction of the fuel consumption and of the environmental impact of avionic flights. All these aspects are becoming increasingly important in our modern society, in which the use of aeroplanes as a transport mean is continuously growing, [2].

Depending on their geometry and on the free-stream flow conditions, swept wings stability and transition can be dominated by four different types of instabilities: stream-wise, attachment line, centrifugal or crossflow, [3]. This work investigates stationary crossflow instabilities (CFI) developing in a low turbulence environment, similar to that of free

*PhD Candidate, Section of Aerodynamics, Faculty of Aerospace Engineering, AIAA Student Member.
†Asossciate Professor, Section of Aeroacoustics, Faculty of Aerospace Engineering
‡Asossciate Professor, Section of Aerodynamics, Faculty of Aerospace Engineering

flight. Crossflow typically develops in the 3D boundary layer of swept wings featuring a favourable pressure gradient. It appears as a set of span-wise periodic co-rotating vortices almost aligned with the free-stream velocity, which grow along the wing chord introducing a progressively stronger modulation of the boundary layer velocity. This in turn gives rise to high frequency secondary instabilities and non-linear effects ultimately causing transition to turbulence, [4–8].

Among the numerous perturbations and non uniformities affecting the free-stream flow, CFI are mainly initiated by the free-stream turbulence level and the three-dimensional roughness of the wing surface, particularly important in the vicinity of the leading edge, [9]. The process through which these external disturbances enter the boundary layer, inducing the instabilities onset and growth, is called receptivity. Previous researches outlined receptivity to free-stream turbulence is fundamental in setting the dominant type of crossflow instability, i.e. [9, 10], but also its interactions with roughness may influence the CFI development, [11, 12]. However, despite the numerous studies conducted, the high sensitivity of the flow to surface roughness has prevented a detailed understanding of its role on wing stability and transition. Nonetheless, both numerical and experimental inquiries demonstrated that suitably arranged DRE arrays can lead to turbulent transition control and delay, behaving like a passive LFC technique, i.e. [4, 5, 13–16]. Still, some late investigations, [17], showed this technique seem to be more effective in wind tunnels than in the real flight environment. This may be due to a not yet clearly defined interaction between the roughness effect and the free-stream turbulence level, and exposes the need of a more in depth study of the receptivity role in the instability onset. The main limitations when addressing this type of investigation come from the numerous parameters and inter-dependencies involved and from the small scales of the phenomena, hardly accessible through experimental techniques. This prevented the experimental investigation of the elements near flow and so of the very first phases of receptivity, hence no direct relation between the forcing configuration and the developing flow features is currently available.

The present study, is dedicated to the investigation of the effect of a wide range of forcing amplitude and chord location on the overall flow stability and transition. In order to define a quantitative relationship between the forcing configuration and the observed downstream evolution of the flow features, the proposed study of CFI exploits simultaneous infra-red thermography (IR) and planar particle image velocimetry (PIV) acquisitions. These measurements allow to correlate the information on the transition front location with the amplitude and shape of the CFI disturbances at various planes along the wing chord. A second objective of the present study is identified in relation to future experimental work. Specifically, the detailed analysis of the evolving instabilities in relation to amplitude and location of roughness elements can provide effective scaling principles. Such scaling can give the possibility of reproducing the swept-wing leading-edge flow features through an up-scaled forcing configuration more tractable in terms of experimental observability. In particular, the investigation of an up-scaled configuration would allow to experimentally resolve the elements near field, essential to clarify the relation between the roughness presence and the cross-flow instability onset, leading to a complete understanding of receptivity.

Hereafter, a description of the experimental set up and applied measurement techniques is reported in section § II, along with the performed stability calculation. Section § III reports instead the results discussion, whose first part deals with the overall stability and transition study, while the latter one is dedicated to a more detailed investigation of the DRE array near-flow.

II. Experimental Set-up

In this section the experimental facility and the equipment used to perform the measures are described along with the main data processing techniques employed.

A. Wing Model and Wind Tunnel Facility

The wind tunnel model studied is an in-house designed swept wing (M3J), fully described in [18], purposely made and already applied at TU Delft to investigate the primary and secondary crossflow instabilities and LFC techniques, [8, 19, 20]. Its geometry is a modification of the NACA 6-series airfoil (66018) designed to achieve a favourable pressure gradient and accelerating flow up to x/c $\simeq$ 0.65 on the pressure side of the model, Figure 1(a). This pressure distribution prevents the development of Tollmien-Schlichting waves, leading to a laminar-to-turbulent boundary layer transition process dominated by crossflow type of instabilities. Moreover, even without the application of wall-liners the model behaves as an infinite-span wing, originating a span-wise invariant flow. Due to the high sensitivity of CFI to surface roughness, the model surface is polished to ensure a contained surface roughness level of $R_q = 0.2\mu$m.

The pressure distribution on the wing pressure side, is measured through two rows of 46 chord-wise distributed pressure taps, located at the 24% and 76% of the wing span. Two different coordinate reference systems are defined for this wing model: one integral with the wind tunnel floor, with spatial components X, Y, Z and velocity components U,

V, W; the second one with z-axis aligned to the leading edge, spatial components x, y, z and velocity u, v, w.

The measurements are performed in the low speed low turbulence wind tunnel (LTT) of the TU Delft, an atmospheric tunnel of closed-throat single-return type. Thanks to the dedicated turbulence screens and the large contraction ratio of 17:1, the free-stream turbulence level in the test section has very low values, reaching intensities around 0.03% for free-stream velocities between 25 to 75 ms^{-1}, [8]. The measurements are performed for α = -3.36° and Re_{c_X} = 2.17×10^6, computed in the free-stream direction and corresponding to $U_\infty \simeq 25 ms^{-1}$. In this conditions the turbulence value is sufficiently low to let stationary crossflow waves dominate the stability and transition scenario, [10, 11]. The background acoustic emissions of the tunnel are not relevant for the transition of crossflow-dominated flow [9, 13].

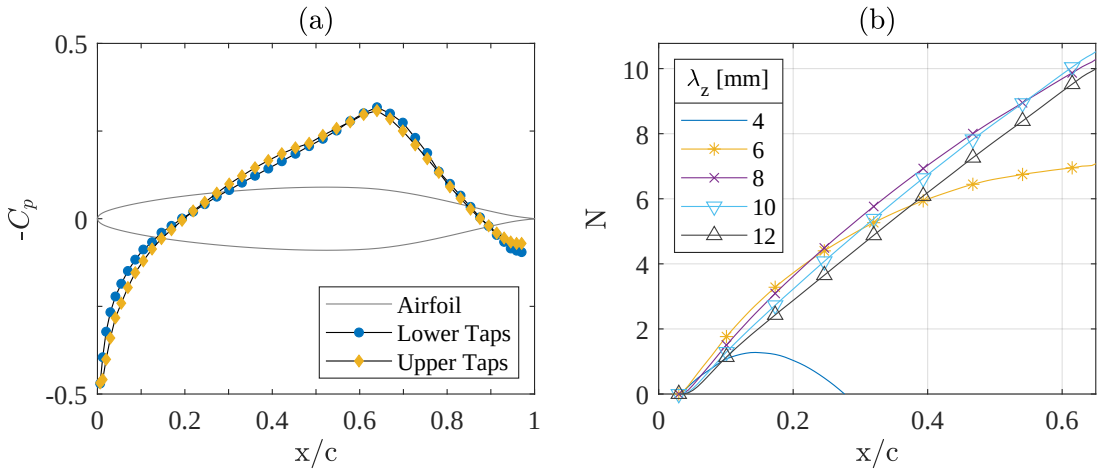

Fig. 1 (a) M3J airfoil geometry orthogonal to the leading edge and pressure distribution measured by the lower (Z = 0.24*b*) and upper (Z = 0.76*b*) arrays of pressure taps at $\alpha = -3.36°$, $Re_{c_X} = 2.17 \times 10^6$. (b) LPSE solution for the experimental reference flow ($\alpha = -3.6°$ and Re_{c_X}=2.17×10^6): N-factor curves evolution in the chord-wise direction for a set of stationary modes with wavelengths λ_z=4-12mm.

B. Numerical Stability Solution

In the present work, a numerical stability solution of the flow is computed through parabolized stability equations (PSE, [21, 22]), an approach frequently applied to the analysis of three-dimnensional boundary layers stability [i.e. 4, 14, 23]. From the wind tunnel pressures acquired at the established test conditions, α = -3.36° and Re_{c_X} = 2.17×10^6, the external velocity of the boundary-layer is estimated and adopted to solve the steady, incompressible and 2.5-dimensional laminar boundary-layer flow, [6, 14, 19]. The instantaneous velocity field is then split in the time independent base flow solution and perturbations. The perturbation variables are described as a combination of a shape function $\hat{q}$ and an exponential wave function (equation 1), and are substituted into the Navier-Stokes equations, [23, 24].

$$\vec{q}'(x, y, z, t) = \hat{q}(x, y) e^{i\left(\int_{x_0}^{x} \alpha(x^*) dx^* + \beta z - \omega t\right)}. \tag{1}$$

Here α and β are the wavenumbers in the stream-wise and span-wise direction respectively, ω is the wave angular frequency, while the integral term accounts for the flow history. Under the assumption of a slowly varying shape function and a rapidly changing wave function in the stream wise direction, the equations can be parabolized, [i.e. 22, 25, 26], and linearized by neglecting the second order terms given by the interaction between different perturbations. However, in equation 1 both α and the $\hat{q}$ are functions of x, hence both functions are capturing growth. Hence, an additional equation is introduced to enforce a mere shape change of $\hat{q}$ transferring all the growth information in α_i: $\int \hat{q}^\dagger \frac{\partial \hat{q}}{\partial x} dy = 0$, where $\hat{q}^\dagger$ is the complex conjugate of mode $\hat{q}$. Once the solution is computed, the amplification N-factor of a mode with wavelength λ_z is defined as the integration of the computed spatial growth rate α_i along the wing chord.

In the present study, the flow stability is solved for the computed base-flow for a combination of stationary modes with given span-wise wavelengths λ_z and a null angular frequency, $\omega = 0$. Hence, the stream-wise wavenumber α is complex with the imaginary part describing the mode growth, while the span-wise wavenumber β is real and is related

to the mode wavelength by $\lambda_z = 2\pi/\beta$. The N-factors computed for a set of wavelengths λ_z=4mm-12mm are presented in figure 1(b). From the LPSE predictions the λ_z=λ_1=8mm mode corresponds to the most amplified mode, as also observed by previous experiments at similar conditions [19, 20]. Confirming the limitations of a linear analysis, this mode is observed to continuously grow between its onset (x/c≃0.03) and x/c=0.65.

These preliminary predictions allow to set the DRE arrays elements inter-spacing, chosen to coincide with the most unstable λ_1 wavelength. Moreover, based on the linear amplification factors, the relevant chord locations for the present DRE receptivity study can be estimated. In particular, locations between x/c=0.02 and x/c=0.35 are considered, with a step of x/c=0.025 chord closed to the leading edge and x/c=0.05 downstream.

C. Span-wise Periodic Discrete Roughness Elements

The numerical solution of the swept wing BL at the chosen test conditions allows to extract all the relevant boundary layer parameters. In particular, to identify the significant DRE height range to test, two geometrical parameters are considered: k/δ^*, the height ratio between the elements and the boundary layer height (represented by the displacement thickness δ^*, [i.e. 27]); and $Re_k = \frac{k \times |\mathbf{u}(k)|}{\nu}$, the roughness Reynolds number [4, 13]. A suitable test matrix is defined starting from their values: arrays of cylindrical elements with a fixed λ_1 inter-spacing and D=2mm diameter but variable heights k (reported in table 1) are applied at the previously defined range of chord locations.

The DRE elements are obtained from the laser cutting of a 100μm thickness black PVC foil. The adhesive side of the foil is strong enough to make the roughness elements adhere to the wing, while allowing their easy removal once the measures are completed. To obtain the higher elements, multiple layers of black foil are pasted on top of each other before starting the cutting procedure. Each element is designed to be cylindrical, however a statistical study is performed to properly characterize their shape and heights. A set of arrays per tested height is scanned trough a scanCONTROL 30xx sensor with a reference resolution of 1.5μm. The extracted values for the elements wavelength, diameter and heights are reported in table 1. In the remainder of this work, the three heights are referenced as k_1, k_2, k_3.

Table 1 Geometric parameters of DRE arrays.

Layers	λ [mm]	λ/λ_1	D [mm]	k [mm]
1	8	1	1.772	0.1147
2	8	1	1.732	0.2179
3	8	1	1.767	0.3292

D. Measurement Techniques and Methodology

Throughout this parametric study, the flow and instabilities development as well as the transition process are globally and locally monitored through infra-red thermography (IR) and planar particle image velocimentry (PIV). The set-up and methodology of both of these applications are described hereafter.

1. Infra-red Thermography

Infra-red thermographic imaging is a non-intrusive measurement technique which acquires the model surface temperatures through specific sensors that capture the IR radiation emitted by a body. In low speed applications as the present study, the aerodynamic body is actively heated by an external device while simultaneously cooled down by the flow through convection, [i.e. 8, 10, 28]. The Reynolds analogy ensures the correspondence between the convective heat flux and the flow shears. Therefore, since the turbulent BL is characterized by higher kinetic energy and wall-shear stress, it leads to an increased surface heat transfer which in turn lowers the surface temperature when compared to laminar BL flows. The temperature difference allows to identify the regions of laminar and turbulent boundary layer flow and consequently the location of the transition front as well as the modulation of the transitional BL induced by the primary stationary CFI.

During this parametric investigation, two Optris PI640 IR cameras image the pressure side of the model through two small openings in the test section vertical side wall. They acquire the surface temperatures at the chosen Reynolds number Re_{c_X}=2.17 $\times$ 10^6 and angle of attack α=-3.36° for different forcing configurations. The cameras have a thermal sensitivity (noise equivalent temperature difference, NETD) of 75 mK given by a 640px $\times$ 480px un-cooled focal plane array (FPA) sensor with 7.5-13μm spectral range. The upstream camera is equipped with a tele-lens of focal length f=18.7mm, and captures a small region of 170 $\times$ 210mm centred at x/c=0.27 and midspan, with spatial resolution of about 0.34mm/px. The downstream camera, features a wider angle lens, f=14.6mm, in order to image a larger portion of the model covering a region 550 $\times$ 400mm centred at x/c=0.23 and midspan with spatial resolution close to 0.85mm/px. Both cameras acquire at a frequency of 4Hz, collecting 80 images that are averaged to improve their signal to noise ratio.

Five halogen lamps (3 × 400W and 2 × 500W) are used to irradiate and warm up the model in order to improve the thermal contrast between the warmer laminar boundary layer region and the colder turbulent region [20]. A sketch of the IR measurements domain and set-up is reported in figure 2(a).

To post-process the IR images an in-house developed routine based on a differential infra-red thermography (DIT) approach is applied, [20, 29]. It inherently accounts for the calibration process, performed by imaging a target stitched on the model surface, introducing the necessary corrections for image distortion and airfoil curvature. During the acquisition, for each forcing case IR images are collected at the reference Reynolds number, $\mathrm{Re}_{c_X} = 2.17{\times}10^6$, and at a higher one, $\mathrm{Re}_{c_X} = 2.7{\times}10^6$. Each couple of corresponding time averaged images, I_A and I_B are then subtracted to define the differential image, namely $I_{DIT} = I_A - I_B$. This technique improves the image quality minimizing the background noise and the possibility of identifying spurious transition fronts. The transition identification procedure, associates the location of the temperature gradient maximum in I_{DIT} to the transition location. Cross-flow dominated transition is usually characterized by an irregular and jagged front, [i.e. 28], therefore a linear fit of the identified span-wise transition front, controlled through suitable confidence bands (corresponding to 95% in this application) is performed to identify the representative transition location.

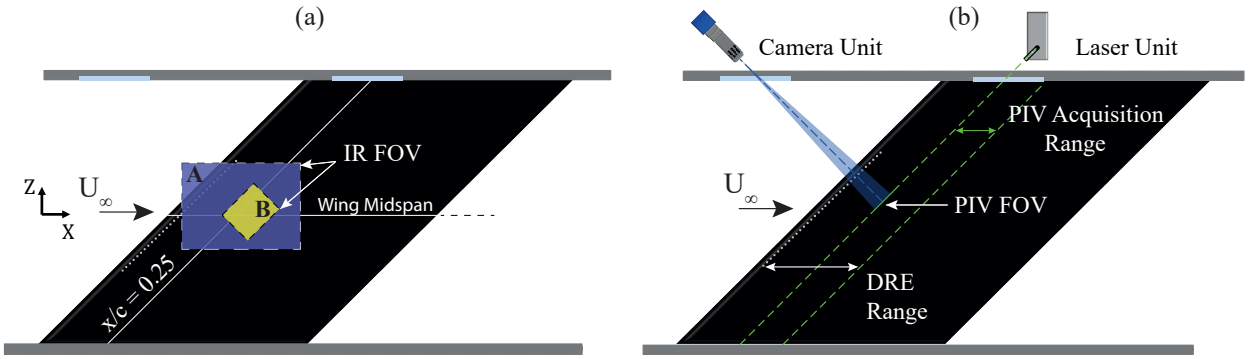

Fig. 2 Sketch of the (a) IR and (b) PIV set-up illustrating the fields of view of the cameras and the location of the PIV laser and imaging system. Flow direction is from left to right, schemes are not to scale.

2. Planar Particle Image Velocimetry

Planar PIV is performed with the objective of describing the flow evolution along the airfoil chord, extracting an estimation of the crossflow vortices growth. The chosen PIV domain extends for almost 40mm (i.e. z/λ_1=5) in the span-wise direction across the model midspan, and for 4mm along the wall normal direction. In the present study, the non-dimensional y is defined as $y/\hat{\delta}^*$ with $\hat{\delta}^* = 6.395 \times 10^{-4}$m being the displacement thickness of the experimentally measured natural boundary layer at x/c=0.25. The PIV domain wall-normal extension ($y/\hat{\delta}^* \simeq 6$) allows to capture the entire boundary layer development in the z-y plane described by $\overline{w}$ and $\overline{v}$, respectively the time-averaged velocity components in the span-wise and wall-normal directions.

The laser and the cameras are mounted on an automated traversing system on top of the section, having optical access to the model through a plexiglass window cut in the upper wall. The laser is a Quantel Evergreen Nd:YAG dual cavity laser (200 mJ pulse energy and λ=532 nm wavelength). Its beam is manipulated through suitable optics and shaped into a sheet propagating along the y direction and aligned to the leading edge. Two LaVision Imager sCMOS cameras (sCMOS, 2560 × 2160 pixels, 16-bit , 6.5μm pixel pitch) are arranged on top of the test section to have a small overlap region, fundamental to join the two fields of view. Moreover, since the wall-region of interest is very small a high magnification factor is obtained applying a Nikon Micro-Nikkor objective featuring a 200 mm focal length lens and two tele-converters to each of the sensors to compensate for the wide distance between the cameras and the wing surface. This results in an 800mm lens whose numerical aperture is set to $f_\# = 8$, corresponding to a magnification ratio of 126px/mm capable of resolving the boundary layer up to the wall vicinity. In Figure 2(b) the laser and cameras arrangement and field of view are sketched. The traversing system is activated to shift the laser and cameras altogether, with an accuracy of 15μm in the displacement: this allows to maintain their alignment and focus while acquiring at different chord locations. With this configuration planes from 25 to 36% of the chord are collected with an inter-spacing of 1% of chord. Dedicated planes with an inter-spacing of $\simeq$ 0.2% chord are also acquired in the vicinity of DRE arrays

applied within the PIV domain, namely configurations with forcing at x_{DRE}/c = 0.25, 0.30, 0.35. Flow seeding is obtained through a SAFEX fog generator by dispersing $\simeq 0.5\mu$m droplets of a water-glycol mixture in the wind tunnel.

At each considered plane, 1000 image pairs are acquired at a frequency of 15Hz. The time shift between two pulses is set to 5μs corresponding to a particle displacement in the free-stream of almost 11 pixels. Each image pair is processed through a multi stage cross-correlation performed using LaVision Davis 10 with final interrogation window of $12\times12 px^2$ with an overlap of 50%, resulting in a final vector spacing of approximately 47μm. The correlated velocity fields are then averaged and joined through a Matlab routine which also identifies the wall as the maximum reflection region in the raw images. The y-axis origin is then shifted in the correspondence of the wall.

The velocity fields are then post-processed to extract the relevant flow features. The boundary layer mean velocity profiles ($\overline{w}_z$) can be obtained by averaging the $\overline{w}$ velocity signal along the z directions. The disturbance evolution profile in the wall-normal direction ($\langle\overline{w}\rangle_z$) is instead computed as the root mean square (rms) of the velocity signal along z at each fixed y-coordinate [i.e. 4, 14]. Information on the dominant mode and its harmonics can be retrieved through a spatial Fourier analysis: at each y coordinate the span-wise velocity signal is transformed in the spatial frequency domain ($\mathrm{FFT}_z(\overline{w})$), allowing to reconstruct the spectra and dominant modes evolution along the chord for different forcing configurations. Moreover, the cross-flow vortices amplitude can be estimated for each acquired plane by integrating the rms disturbance profiles along y, as suggested by [4, 11], or considering the rms profile maximum amplitude as [14, 23]. This gives estimation of the modes growth and evolution along the airfoil chord, as discussed in § III.B.

Along with the velocity fields, the correlation procedure in DaVis10 allows to quantify the uncertainty of the estimated displacement field through the correlation statistics method proposed by [30]. An overall average value of the uncertainty can be computed as the average of the uncertainty of all the vectors. Normalising this value by the free-stream velocity W_∞, the uncertainty is estimated to be approximately 0.05% (0.0097m/s) in the free-stream and 0.10% (0.0195m/s) inside the boundary layer region.

III. Results

This section is dedicated to the discussion of the stationary disturbances onset and evolution based on the IR and PIV measurements. In §III.A and §III.B a general overview of the flow receptivity to the roughness arrays is reported, while a more in depth investigation of the flow characteristics in the vicinity of the DRE arrays is described in §III.C.

A. Transition Behaviour as Function of Forcing Amplitude and Location

The acquired IR thermography data provide a representation of the overall flow stability and transition under the effect of the various boundary layer forcing configurations tested. The transition front location can be extracted from the acquired IR images for all measured cases. Figure 3(a), shows the transition location x_{TR}/c modifications for changes in the DRE chord location x_{DRE}/c, and amplitude k. The clean wing case transition lays outside the IR domain, most likely around $x/c \simeq 0.65$ according to the numerical stability solution, so is not included in this graph. Figures 3(b-d) report the infra-red images acquired for three different forcing cases chosen as representative for the effect of a DRE amplitude or location change. All three acquisitions display the characteristic light-dark streaks approximately aligned to the stream-wise direction typical of IR acquisition of cross-flow dominated boundary layers [i.e 28]. Their presence is considered as the footprint of stationary cross-flow vortices on the wing surface. Moreover, figures 3(b) and (d) display an evident temperature difference between the upstream and downstream portion of the domain, which allows to easily distinguish the saw-tooth pattern of the transition front [i.e. 5, 28].

Figure 3(a), show that the set of collected data identifies two main trends in the transition front behaviour. Namely, keeping a fixed element height, a downstream shift of the DRE array is accompanied by a downstream shift of transition. This reflects the high sensitivity of the flow to surface features in the vicinity of the leading edge, which is expected to reduce moving past the dominant mode neutral point [i.e. 17]. On the other hand, an increase of DRE height at a fixed chord location leads to a transition advancement. This is partially explained by the fact that a higher element is expected to originate instabilities with higher initial amplitude, thus advancing the stages of growth, saturation and breakdown. Figure 3(a) also shows the smaller k_1 and k_2 describe similar trends as the arrays are shifted along the chord. They can both be identified as *critical* in the range x/c=0.02-0.20, since they affect the flow without causing direct tripping in the array vicinity. The k_3 element, is instead observed to cause transition in correspondence of the array location when applied closed to the leading edge. Therefore it is considered *super-critical* up to x/c=0.075, while it behaves critically between x/c=0.075-0.3 showing a trend comparable to the other elements. Finally, all the tested arrays show a *sub-critical* behaviour after a specific chord location, having a negligible effect on the overall flow development.

However, despite the monotonic trends identified, the transition location modifications due to DRE location and

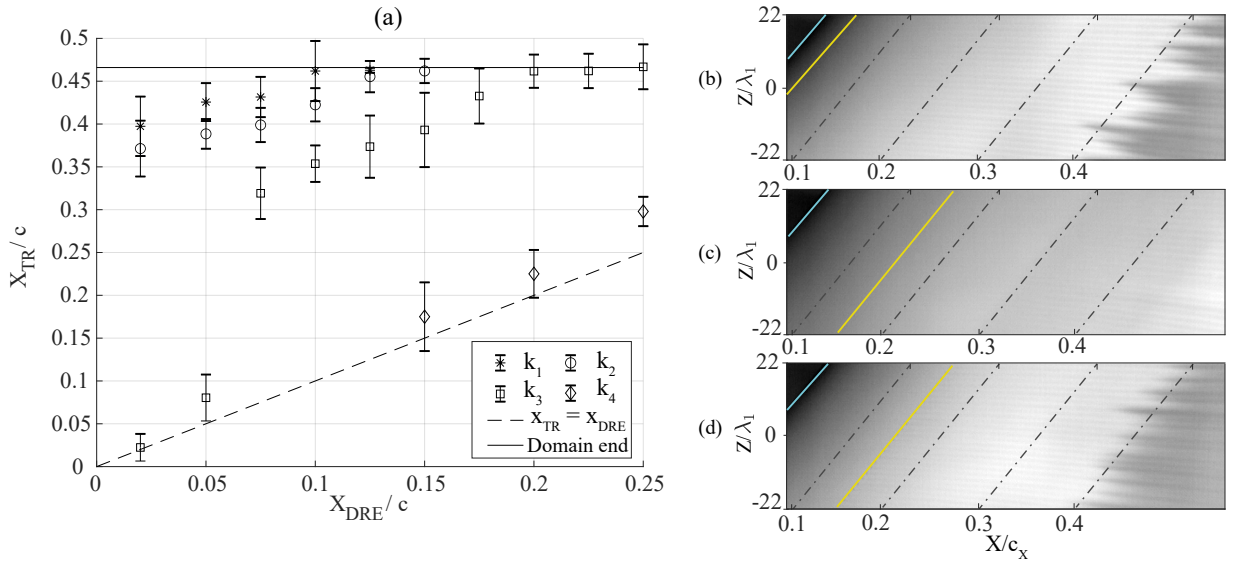

Fig. 3 (a) Map of transition locations x_{TR}/c extracted from IR visualization fields at $\alpha = -3.36°$ and $Re_{c_X} = 2.17 \times 10^6$ for different forcing. The error bars represent the minimum and maximum extent of laminar flow in the measured configuration. The black dashed line (- -) represents the arrays causing transition in correspondence of their location of application, while the continuous black line (–) represents the edge of the IR domain. *Right* IR acquisition for forcing at (b) x_{DRE}/c=0.05, k_1; (c) x_{DRE}/c=0.15, k_1; (d) x_{DRE}/c=0.15, k_3. The light blue line represents the leading edge while the yellow one the array location.

amplitude are not simply linear. In particular, at fixed forcing amplitude the chord-wise distance between the DRE location and the transition location is almost constant. The amplitude modifications, instead, are associated to alterations of the flow and of the instabilities development induced by the specific forcing configuration applied, as can be further investigated considering the collected PIV data.

Figure 4 shows the contours of the time-averaged span-wise $\overline{w}$ velocity component at x/c=0.25, 0.30 and 0.35, again representative for a downstream shift of the array and a height increase of the elements. The acquired PIV domain

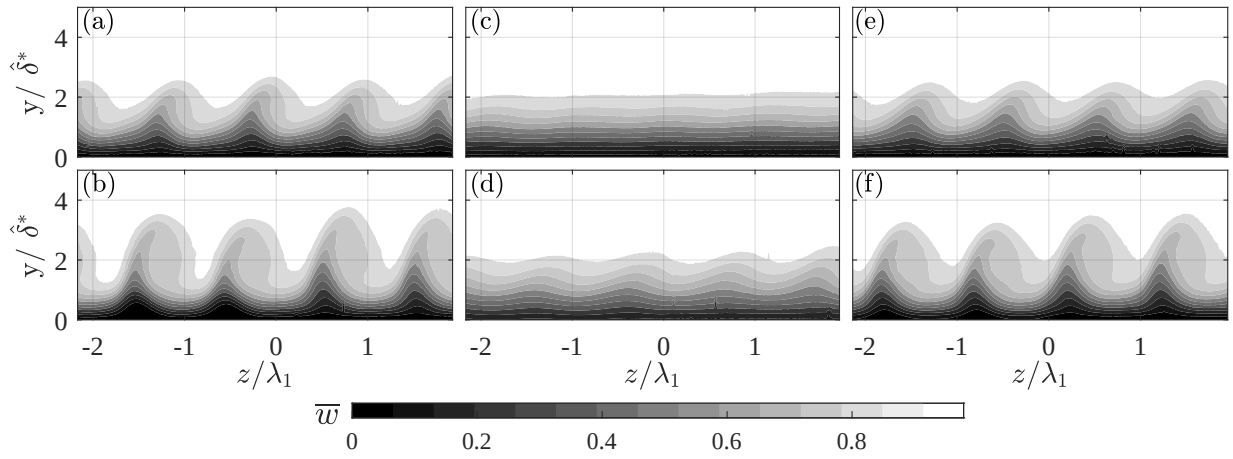

Fig. 4 Contours of time-averaged span-wise $\overline{w}$ velocity at $\alpha = -3.36°$ and $Re_{c_X} = 2.17 \times 10^6$ with different forcing. (a-b) x_{DRE}/c=0.05, k_1; (c-d) x_{DRE}/c=0.15, k_1; (e-f) x_{DRE}/c=0.15, k_3. Rows refer to a specific PIV plane of acquisition: *Top* x/c=0.25; *Bottom* x/c=0.35.

includes four periodically spaced vortices with an inter-spacing close to λ_1 and pictures the whole boundary layer development up to the free-stream. Moreover, the four vortices appear closely alike in the flow, confirming the desired span-wise invariance is achieved with this set-up despite the absence of wall liners. The reported velocity contours allow to qualitatively characterize the cross-flow disturbances and their evolution, which reflect the previously observed trends: a downstream shift of the array is reducing their intensity delaying transition, while a higher height is enhancing them anticipating also the turbulence onset. A more quantitative interpretation of modes growth and evolution can be achieved through Fourier and amplitude analysis as discussed in the following sections.

B. Crossflow Instabilities Growth

To retrieve detailed information on the dominant mode λ_1 and its harmonics, the velocity fields can be analysed through a spatial Fourier decomposition: at each y coordinate the span-wise velocity signal is transformed in the spatial frequency domain ($\mathrm{FFT}_z(\overline{w})$), allowing to reconstruct the spectra and dominant modes along the chord for different forcing configurations. When applied to all the collected PIV planes, this procedure allows to extract information on the single modes evolution along the chord for each forcing case.

For sake of brevity, only one representative configuration is reported, namely x_{DRE}/c = 0.05, k_1. Its spatial spectra along with the corresponding spectra-peaks contours in the x-λ_z plane are shown in figure 5. The dominant peak corresponds to the λ_1 mode which can be seen to grow up to x/c =0.33, saturating afterwards due to non-linear interactions between the dominant cross-flow mode and its harmonics. In fact, besides the λ_1 peak, the spectra shows significant amplitudes for the λ_2=λ_1/2 and λ_3=λ_1/3 modes, respectively corresponding to the second and third harmonics of the dominant mode, also growing along the wing chord.

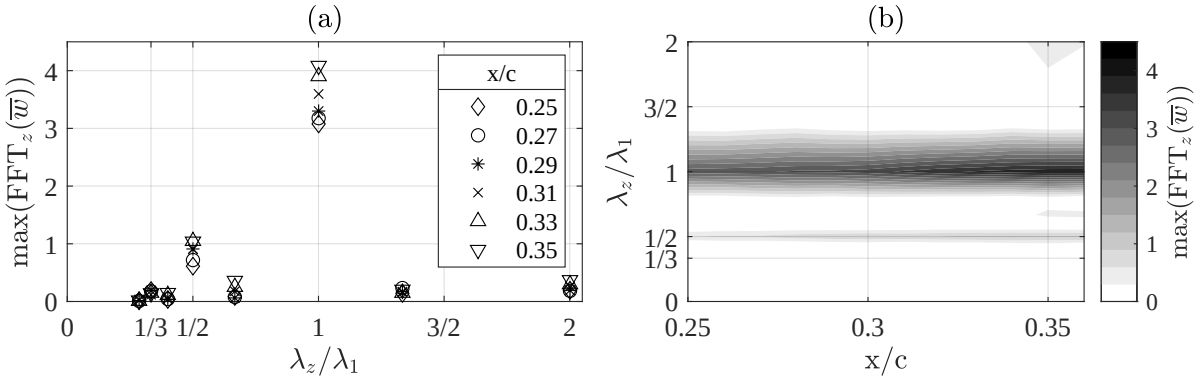

Fig. 5 (a) Fourier spectra in the spatial (wavelength) domain and (b) spectra amplitudes contours in the x-λ_z plane extracted through Fourier analysis of the time-averaged PIV velocity fields acquired at $\alpha = -3.36°$ and $\mathrm{Re}_{c_X} = 2.17 \times 10^6$ for forcing at x_{DRE}/c=0.05, k_1.

From this spatial Fourier decomposition, every mode can be independently extracted, hence an inverse Fourier transformation allows to reconstruct the time-averaged velocity fields as only composed by the mean flow and a chosen truncated ensemble of modes of interest. In this way, the effect of each mode and its evolution can be isolated and analysed by processing the corresponding reconstructed flow fields. The reconstructed velocity fields are indicated as $\overline{w}_{R_i}$ where the subscript R stands for *reconstructed*, and i indicates which modes are included. In figure 6 are reported the disturbance velocity profiles $\langle\overline{w}\rangle_z$ computed for the reference forcing case, compared with the disturbance profiles extracted from two FFT reconstructed fields: $\overline{w}_{R_1}$ including only the base flow plus the λ_1 mode and $\overline{w}_{R_{1,2,3}}$ also accounting for λ_2 and λ_3 harmonics. At all the considered chord locations, the three disturbance profiles look similar in shape. Downstream of x/c=0.25, they all feature a secondary local maxima related to non-linear interactions. However, their maximum amplitude slightly differs, being higher for the PIV-computed disturbances that account for all the contributions to the flow distortion. The discrepancy progressively reduces as more modes are included in the FFT flow reconstruction, even if the mild differences between the two reconstructed profiles confirm the dominance of the λ_1 mode. Moreover, only the disturbance profiles coming from the Fourier reconstructed velocity fields reach the expected null value in the free-stream, suggesting they are more indicated for the detailed study of the modes growth. As considering their chord-wise evolution, an increase in both maximum amplitude and wall-normal extension of

the profiles is observable, revealing the corresponding flow structures are not only growing in intensity but also in dimensions as the boundary layer thickens.

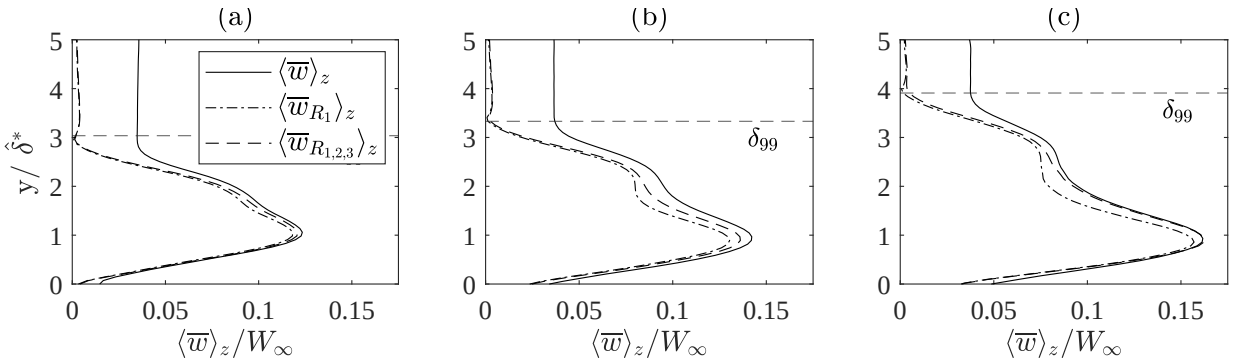

Fig. 6 Experimental boundary layer disturbance profiles computed at different chord locations from PIV fields at $\alpha = -3.36°$ and $Re_{c_X} = 2.17 \times 10^6$ with forcing at x_{DRE}/c=0.05, k_1. Comparison between profiles extracted from the original time-averaged PIV fields $\langle\overline{w}\rangle_z$ (–) and two Fourier reconstructed fields $\langle\overline{w}_{R_1}\rangle_z$ (-.) and $\langle\overline{w}_{R_{1,2,3}}\rangle_z$ (- -). All disturbance profiles are normalized by W_∞. Dashed black lines represent the experimental δ_{99}.

Two different approaches have been proposed in past studies to quantify the disturbance amplitudes. By extracting the maximum value of the $\langle\overline{w}\rangle_z$ disturbance profile at each chord location [4, 14] a maximum amplitude value can be estimated, further indicated as A_{max} and non-dimensionalized by the free-stream speed W_∞. An integral amplitude can be instead defined integrating the $\langle\overline{w}\rangle_z$ profiles in the wall-normal direction up to $y = \delta_{99}$ for each acquired plane to obtain $A_{int} = \frac{1}{\delta_{99} * W_\infty} \int_0^{\delta_{99}} \langle\overline{w}\rangle_z(y)dy$, [11]. Both approaches can either be applied to the original PIV fields or to their $\overline{w}_{R_1}$ Fourier reconstruction, which allows to isolate the λ_1 mode growth while reproducing all the relevant disturbance characteristics. Figure 7(a) compares the 4 resulting curves computed for the x_{DRE}/c=0.05, k_1 forcing case. The differences between the PIV and FFT estimations are minimal, confirming the λ_1 mode gives the main contribution to the amplitude and its development. On the other hand, significant differences appear between the two estimation procedures, with the maximum amplitude showing lower growth as also confirmed by figure 7(b) reporting the $\widetilde{N} = ln(\frac{A}{A_{25\%}})$ curves, where $A_{25\%}$ is the amplitude value measured at x/c=0.25 for each configuration. The relevant differences between the integral and maximum amplitude curves can be explained by the well-developed cross-flow

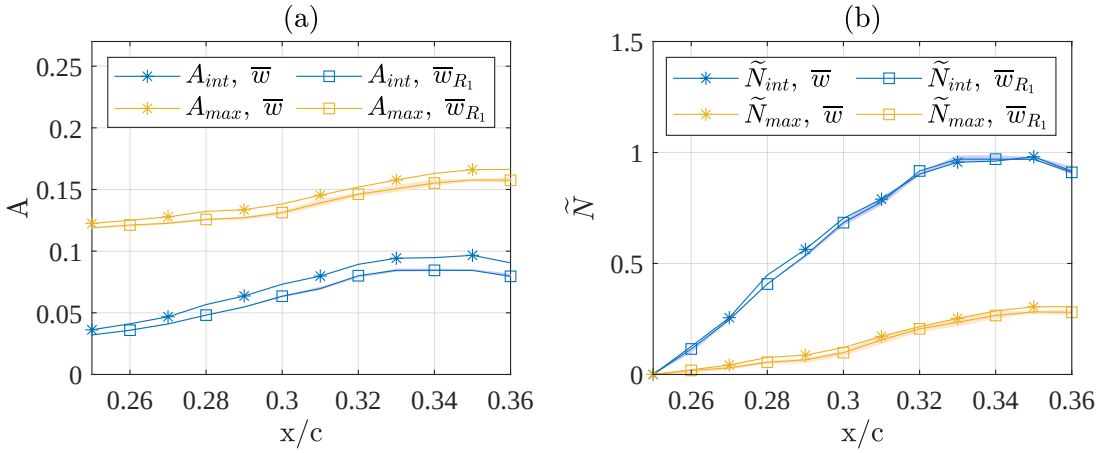

Fig. 7 (a)Amplitude and (b) $\widetilde{N}$ trends along the wing chord, computed from PIV acquisitions at $\alpha = -3.36°$ and $Re_{c_X} = 2.17 \times 10^6$ for forcing at x_{DRE}/c=0.05, k_1. Comparison between integral amplitudes A_{int} (blue lines) and maximum amplitudes A_{max} (yellow lines) extracted from $\overline{w}$ (∗) and from $\overline{w}_{R_1}$ (□) fields. Shadowed areas in represent the PIV error propagation in the amplitude calculation (only reported for the $\overline{w}_{R_1}$ fields).

instabilities characterizing the considered forcing case. In fact, from the very beginning of the experimental domain a secondary lobe and so non-linearities are developing, justifying the mild growth or even the saturation of the main peak amplitude along the considered portion of chord. Correspondingly the A_{max} undergoes small changes and mild growth throughout the domain. The second lobe, however, is also subject to growth along the chord and these modifications are captured by the A_{int} estimation, since it considers the whole rms profile.

At last, an estimation of the PIV error propagation in the amplitude curves is performed starting from the DaVis10 calculation of the instantaneous uncertainty fields and their average [30]. Two additional flow fields are built by adding or subtracting the uncertainties from the time-averaged PIV fields, and are processed through the Fourier reconstruction and amplitude extraction routine to estimate both the A_{max} and A_{int} curves. Their differences provide an error range for the amplitude calculation with mean value of ±1.2%. Based on the comparable acquisition and processing configurations, these estimations are considered representative for the PIV errors affecting all tested configurations.

Considering the previous observations, the amplitude curves presented hereafter are extracted from the Fourier reconstructed flow fields, both $\overline{w}_{R_1}$ and $\overline{w}_{R_2}$, following the maximum amplitude procedure. The effect of different forcing cases can be outlined comparing the evolution of the disturbances they generate. The most upstream array considered, i.e. x_{DRE}/c = 0.02, k_1, shows a different behaviour with respect to the other k_1 and k_2 cases. In fact, it achieves higher amplitude values throughout the whole PIV up to a peak value around x/c =0.32, but decays further downstream also followed by the λ_2 mode. The rapid decrease of amplitude downstream of x/c=0.32 is representative of the later stages of transition and onset of turbulence, which essentially breaks the span-wise coherence of the structures. A comparable behaviour is observed for the first three chord locations tested with the k_3 arrays, namely x_{DRE}/c =0.075, 0.1 and 0.125, which introduce instabilities with higher initial amplitude and growth rate developing turbulence and early transition. The other leading edge configurations, x_{DRE}/c =0.05 and 0.075 for k_1, show a monotonic growth up to a saturation amplitude, a behaviour mirrored also by the arrays of higher elements, k_2 at x_{DRE}/c =0.05, 0.075 or

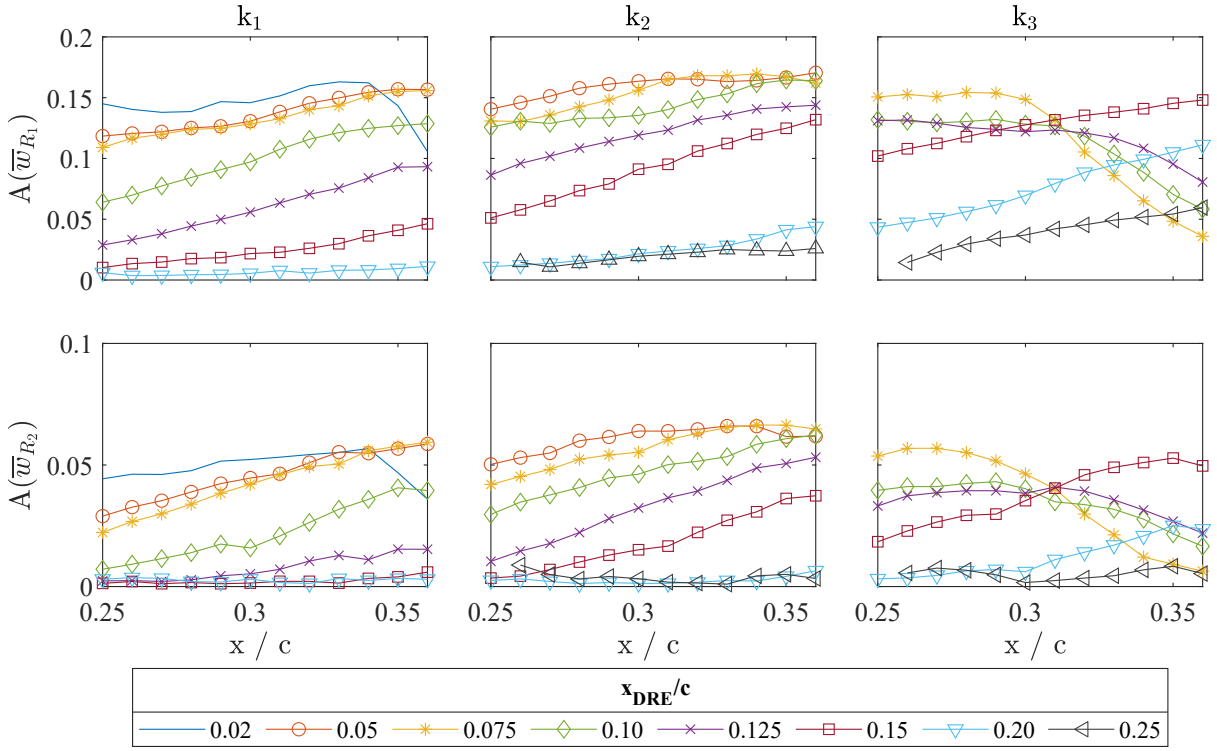

Fig. 8 Amplitude trends along the wing chord, computed from PIV acquisitions at $\alpha = -3.36°$ and $Re_{c_X} = 2.17 \times 10^6$ for different forcing configurations following the A_{max} procedure. Columns refer to a fixed elements height: *Left* k_1; *Center* k_2; *Right* k_3. *Top* row, amplitudes computed on Fourier reconstructed fields containing only the base flow and the dominant λ_1 mode; *Bottom* row amplitudes computed on Fourier reconstructed fields containing only the base flow and the first λ_2 harmonic.

0.1. In agreement with what observed by previous studies [i.e. 4, 31], for this sub-set of cases, the forced primary structures reach saturation at comparable amplitude values ($\simeq 0.16 W_\infty$) independently of the forcing amplitude and location. All these cases are accompanied by the monotonic growth of the λ_2 mode, which also saturates for the more upstream configurations. However, forcing at more downstream chord locations as well as with higher k_3 arrays, leads to saturation at smaller amplitudes. This different behaviour can be attributed to several reasons, among which the width of the parameter range involved which may lead to variations in the receptivity process. With a further downstream shift, arrays of all considered heights induce instabilities that monotonically grow along the domain while achieving overall smaller amplitudes. The majority of these cases do not show saturation within the domain, and are accompanied by a negligible or absent development of the λ_2 mode.

Overall, the reported amplitude curves reflect the previously observed instability behaviours, with stronger CFI originating for upstream forcing locations or higher elements. However, the relation between the applied forcing configuration and the developing instability amplitudes is again far from linear. This suggests that non-linear flow features may be developing in the elements near wake, affecting the instability onset and its subsequent development. Therefore, a further step towards the analysis of the relation between the DRE element and the initial instability amplitude can be guided by the elements near flow investigation, briefly reported in §III.C.

C. DRE Elements Near Flow

To further investigate the initial phases of receptivity leading to the instability onset, the last part of this work is dedicated to a more in depth analysis of the flow evolution in the vicinity of the roughness elements. In fact, for arrays applied between x/c=0.25-0.35 some PIV planes are collected with a step of 2mm ($\simeq$ 0.2% chord) starting starting 0.3% chord aft of the elements to avoid light reflections.

The time-averaged span-wise $\overline{w}$ velocity contours for a reference case with forcing at x_{DRE}/c=0.25, k_2 are reported in figure 9. These fields are characterized by a boundary layer almost unaffected by cross-flow, in fact no modulation is yet visible in the base flow at x/c=0.253. However, a low speed hump is forming in the flow region corresponding to the elements wake. Already visible in the closest plane presented (x/c=0.253), the low-speed hump appears to be stronger close to the array while it decays as moving downstream between x/c=0.253-0.26. Downstream of x/c=0.27, the humps level out and a weak but uniform flow modulation is visible in their place. This modulation is due to cross-flow development, in fact it is dominated by the λ_1 mode, and grows downstream reflecting the previously observed trends. These considerations can be related to the direct numerical simulations (DNS) results by [32], who identified two pairs of horseshoe vortices developing around the roughness elements. In particular, an outer vortex pair is propagating from

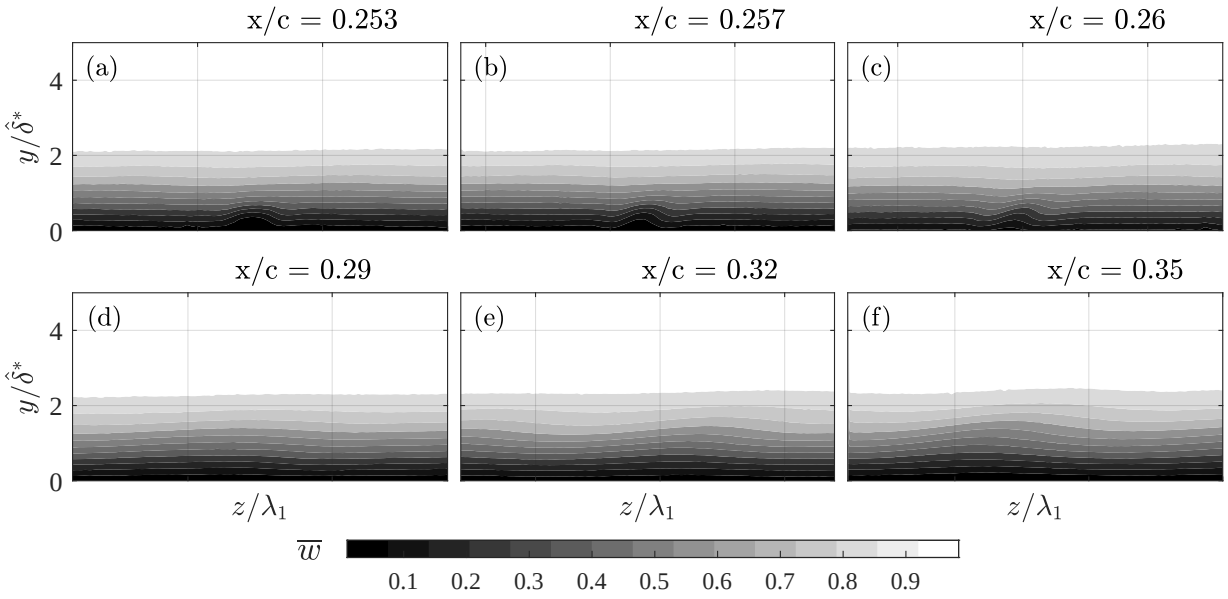

Fig. 9 Contours of time-averaged span-wise $\overline{w}$ velocity field acquired in the close vicinity of the DRE array at $\alpha = -3.36°$ and $Re_{c_X} = 2.17 \times 10^6$ for forcing at x_{DRE}/c=0.25, k_2.

the element sides, most likely due to the span-wise shear, while an inner vortex pair originates aft of the element due to wall-normal ejection of flow. In a three-dimensional boundary layer, for both pairs only the leg co-rotating with the cross-flow is sustained and develops along the chord, while the others are suppressed shortly after the elements location. Their presence origins a momentum redistribution process which results in the formation of a low-speed hump in the wake of the elements due to low-momentum flow up-welling.

The presented spatial Fourier decomposition is applied also to these fields, and the corresponding spectra are reported in figure 10(a). Differently from the upstream forcing case of figure 5, the reported spectra contours show that the element vicinity is characterized by a high spectral content involving the dominant mode λ_1 and numerous harmonics. This suggests that non-linear and possibly non-modal effects may be dominating the near wake flow development. Therefore, the amplitude disturbance for these cases is computed following the integral approach, such that all the complex flow features corresponding to the near wake development can be included, figure 10(b). The resulting amplitude curves feature a rapid amplitude decay immediately after the element possibly linked to the low-speed hump evolution, while an amplitude growth follows shortly after due to the cross-flow onset and evolution.

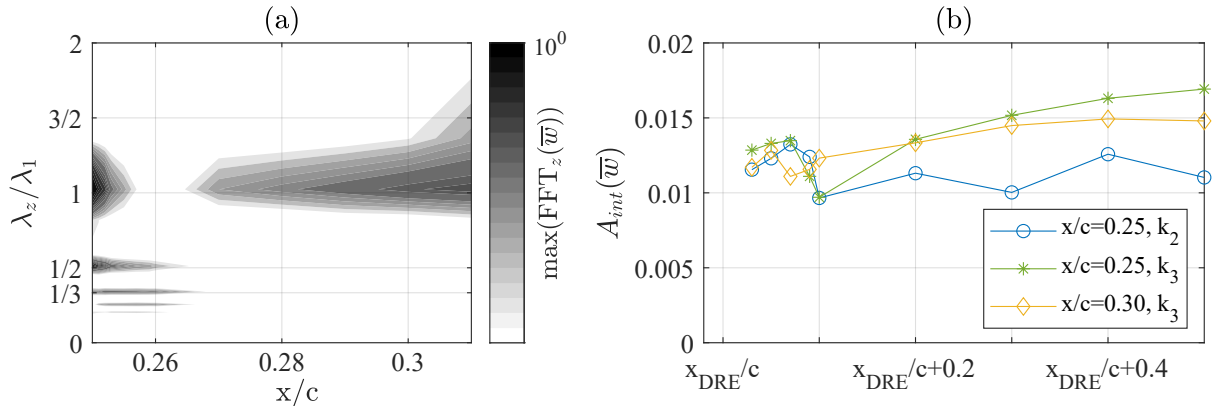

Fig. 10 (a) Fourier spectra evolution in the x-λ_z domain extracted in the close vicinity of the DRE array for velocity fields acquired for forcing at x_{DRE}/c=0.25, k_2. (b) Amplitude trends computed in the close vicinity of the DRE array following the A_{int} procedure on $\overline{w}$ fields with different forcing.

Even if a clear explanation for the observed behaviour is difficult to extrapolate from the few investigated cases, the decay and growth trends of the amplitude curves appear to be mostly unaffected by a change of the forcing location. This suggests that the near-flow region is mostly influenced by the flow blockage caused by the element rather than by the overall flow stability, in agreement with the results of [15, 32]. Additionally, the investigation of the x_{DRE}/c=0.30, k_3 forcing, is also validating this behaviour. In fact, for this downstream forcing configuration no additional conditioning of the flow is performed close to the leading edge. Therefore, the boundary layer naturally evolves on the wing up to x/c≃0.30. The investigation of the natural flow at x/c=0.29 shows that even if a wide band of modes is excited, a mild λ_1 mode is dominating the boundary layer introducing a mild modulation. Therefore, DRE array is applied in a region already affected by weak CFI. Nonetheless, the instability amplitude reconstruction shows that when the natural flow interacts with the array, the dominant flow features become those developing in the elements wake, [15]. The low speed humps in fact, still develop behind the elements and decay shortly downstream (figure 10). However, downstream of the near-flow region (x/c≃0.27), the λ_1 modulation is again characterizing the flow with increasing amplitude along the wing chord rapidly becoming the dominant instability. Hence, despite the smaller instability amplitudes involved, the boundary layer conditioning appears to be effective also when performed at this downstream chord location.

However, the reported observations suggest that the withstanding relation between roughness elements and cross-flow onset may be more complex than a simple two elements interaction. Instead, it possibly involves a chain of effects which first connect the roughness elements to their near wake flow, and subsequently lead to the CFI onset. Considering their relevant role in the complete definition of the receptivity process, these relations will be the subject of future investigations dedicated to the near element flow features. These investigations can be simplified by the observed repeatability of the near wake characteristics, which allows to perform the near flow measurements at more downstream and experimentally more accessible chord locations.

IV. Conclusions

The presented experimental study is conducted to investigate the overall effect of discrete roughness elements height and chord location on the development and breakdown of stationary CFI. Roughness arrays are manufactured with a fixed wavelength, corresponding to the one of the dominant cross-flow mode (λ_1), and four heights k. They are then applied on the swept-wing model surface at different chord locations to force the development of monochromatic instabilities in the wing boundary layer.

The global flow investigation performed through IR thermography allows to identify some overall trends and behaviours. In particular, a downstream shift of the array location corresponds to a downstream shift of the transition front of almost the same entity. The element height increase, is instead causing a transition advancement due to the introduction of instabilities with enhanced initial amplitude and so development and breakdown. Moreover, all considered heights display a critical or sub-critical behaviour depending on the chord location of application. The higher k_2 and k_3 also behave super-critically when applied in the leading edge vicinity.

A quantitative investigation of the instabilities development is provided by the PIV acquisitions. Through a spatial Fourier decomposition, the spectral content of the velocity fields is analysed and the dominant λ_1 mode and its harmonics can be isolated and independently studied. In particular, the reconstruction of the flow fields based on the summation of the base flow and a chosen ensemble of modes, proves that all the main flow features can be captured by the λ_1 mode. Therefore, from the reconstructed $\overline{w}_{R_1}$ flow fields, the maximum instability amplitude of the dominant mode is estimated along the wing chord. Reflecting the transition modifications, an upstream forcing configuration or a higher element forcing introduce instabilities with higher amplitude, which keep growing along the chord up to saturation and turbulence onset. As observed in previous studies [4, 23], the more upstream forcing cases are characterized by a saturation amplitude almost independent from the forcing configuration. As considering the wider range of considered parameters however, this behaviour is not repeatable, likely because of the complexity of the receptivity process.

At last, the element near flow is investigated. The velocity contours allow to identify the presence of a low speed hump located in correspondence of the element wake, [32]. This hump is present aft of the element, however decays further downstream while a cross-flow due boundary layer modulation (dominated by λ_1 mode) develops. This flow features are reflected by the amplitude estimations, which undergo a rapid decay in the element vicinity, but start growing at more downstream chord locations due to the CFI onset. Additionally, the application of DRE in a region mildly affected by the natural CFI development is still conditioning the cross-flow development. On the other hand, the pre-existing CFI modulation appears to have negligible effects on the near wake features, which present comparable amplitude and behaviour independently of the forcing chord location, [15].

Therefore, the withstanding relation between roughness elements and cross-flow onset may be more complex than a simple two elements interaction, involving instead a chain of effects moving from the elements to their near wake flow and consequently to the onset of the CFI. Considering their relevant role in the complete definition of the receptivity process, these relations will be further investigated through dedicated set-up simplified by the observed repeatability of the near wake characteristics. In fact, this would allow to perform the near element flow measurements at more downstream and experimentally more accessible chord locations.

Acknowledgments

This research is conducted under the financial support of ERC through the GLOWING Project. The authors express their gratitude to S.Bernardy, E.Langedijk sharing their technical knowledge during the experimental preparation. A special thank you goes to K.Peng and A. Vidales, for their contribution and support during these experiments.

References

[1] Arnal, D., and Archambaud, J. P., "Laminar-turbulent Transition Control: NLF, LFC, HLFC," *Advances in Laminar-Turbulent Transition Modeling*, 2008.

[2] Airports Council International, A., "Preliminary world airport traffic rankings," , 2018.

[3] Saric, W. S., Reed, H. L., and White, E. B., "Stability and transition of three dimensional boundary layers," *Annual Review of Fluid Mechanics*, Vol. 35, No. 1, 2003, pp. 413–440. https://doi.org/10.1146/annurev.fluid.35.101101.161045.

[4] Reibert, M., Saric, W. S., R. Carrillo, J., and Chapman, K., "Experiments in nonlinear saturation of stationary crossflow vortices in a swept-wing boundary layer," *34th Aerospace Sciences Meeting and Exhibit*, American Institute of Aeronautics and Astronautics, 1996. https://doi.org/10.2514/6.1996-184.

[5] Saric, W. S., Carrillo, R., and Reibert, M., "Leading-edge roughness as a transition control mechanism," , 1998. https://doi.org/10.2514/6.1998-781.

[6] Malik, M. R., Li, F., Choudari, M. M., and Chang, C. L., "Secondary instability of crossflow vortices and swept-wing boundary-layer transition," *Journal of Fluid Mechanics*, Vol. 399, 1999, pp. 85–115. https://doi.org/10.1017/s0022112099006291.

[7] Bonfigli, G., and Kloker, M., "Secondary instability of crossflow vortices: validation of the stability theory by direct numerical simulation," *Journal of Fluid Mechanics*, Vol. 583, 2007, pp. 229–272. https://doi.org/10.1017/s0022112007006179.

[8] Serpieri, J., "Cross-Flow Instability," Ph.D. thesis, 2018. https://doi.org/10.4233/UUID:3DAC1E78-FCC3-437F-9579-048B74439F55.

[9] Deyhle, H., and Bippes, H., "Disturbance growth in an unstable three-dimensional boundary layer and its dependence on environmental conditions," *Journal of Fluid Mechanics*, Vol. 316, 1996, pp. 73–113. https://doi.org/10.1017/s0022112096000456.

[10] Bippes, H., "Basic experiments on transition in three-dimensional boundary layers dominated by crossflow instability," *Progress in Aerospace Sciences*, , No. 35, 1999, pp. 363–412.

[11] Downs, R. S., and White, E. B., "Free-stream turbulence and the development of cross-flow disturbances," *Journal of Fluid Mechanics*, Vol. 735, 2013, pp. 347–380. https://doi.org/10.1017/jfm.2013.484.

[12] Kurian, T., Fransson, J. H. M., and Alfredsson, P. H., "Boundary layer receptivity to free-stream turbulence and surface roughness over a swept flat plate," *Physics of Fluids*, Vol. 23, No. 3, 2011, p. 034107. https://doi.org/10.1063/1.3562843.

[13] Radeztsky, R. H., Reibert, M. S., and Saric, W. S., "Effect of Isolated Micron-Sized Roughness on Transition in Swept-Wing Flows," *AIAA Journal*, Vol. 37, No. 11, 1999, pp. 1370–1377. https://doi.org/10.2514/2.635.

[14] Tempelmann, D., Schrader, L. U., Hanifi, A., Brandt, L., and Henningson, D. S., "Swept wing boundary-layer receptivity to localized surface roughness," *Journal of Fluid Mechanics*, Vol. 711, 2012, pp. 516–544. https://doi.org/10.1017/jfm.2012.405.

[15] Kurz, H. B. E., and Kloker, M. J., "Receptivity of a swept-wing boundary layer to micron-sized discrete roughness elements," *Journal of Fluid Mechanics*, Vol. 755, 2014, pp. 62–82. https://doi.org/10.1017/jfm.2014.425.

[16] Saric, W. S., Carpenter, A. L., and Reed, H. L., "Passive control of transition in three-dimensional boundary layers, with emphasis on discrete roughness elements," *Philosophical Transactions of the Royal Society A: Mathematical, Physical and Engineering Sciences*, Vol. 369, No. 1940, 2011, pp. 1352–1364. https://doi.org/10.1098/rsta.2010.0368.

[17] Saric, W. S., West, D. E., Tufts, M. W., and Reed, H. L., "Experiments on discrete roughness element technology for swept-wing laminar flow control," *AIAA Journal*, Vol. 57, No. 2, 2019, pp. 641–654. https://doi.org/10.2514/1.j056897.

[18] Serpieri, J., and Kotsonis, M., "Design of a swept wing wind tunnel model for study of cross-flow instability," *33rd AIAA Applied Aerodynamics Conference*, American Institute of Aeronautics and Astronautics, 2015. https://doi.org/10.2514/6.2015-2576.

[19] Serpieri, J., and Kotsonis, M., "Three-dimensional organisation of primary and secondary crossflow instability," *Journal of Fluid Mechanics*, Vol. 799, 2016, pp. 200–245. https://doi.org/10.1017/jfm.2016.379.

[20] Vidales, A. F. R., Kotsonis, M., Antunes, A. P., and Cosin, R., "Effect of Two-Dimensional Surface Irregularities on Swept Wing Transition: Forward Facing Steps," *2018 Fluid Dynamics Conference*, American Institute of Aeronautics and Astronautics, 2018. https://doi.org/10.2514/6.2018-3075.

[21] Simen, M., "Local and non-local stability theory of spatially varying flows," *Instability, Transition, and Turbulence*, Springer, 1992, pp. 181–201.

[22] Herbert, T., "Parabolized stability equations," *Annual Review of Fluid Mechanics*, Vol. 29, No. 1, 1997, pp. 245–283.

[23] Haynes, T., and Reed, H., "Simulation of swept-wing vortices using nonlinear parabolized stability equations," *Journal of Fluid Mechanics*, Vol. 405, 2000, pp. 325–349. https://doi.org/10.1017/s0022112099007260.

[24] Herbert, T., "Parabolized Stability Equations." *AGARD: Special Course on Progress in Transition Modelling, AGARD-R-d793*, 1993.

[25] Bertolotti, F. P., Herbert, T., and Spalart, P. R., "Linear and nonlinear stability of the Blasius boundary layer," *Journal of Fluid Mechanics*, Vol. 242, 1992, pp. 441–474. https://doi.org/10.1017/s0022112092002453.

[26] Tempelmann, D., Hanifi, A., and Henningson, D. S., "Spatial optimal growth in three-dimensional compressible boundary layers," *Journal of Fluid Mechanics*, Vol. 704, 2012, pp. 251–279. https://doi.org/10.1017/jfm.2012.235.

[27] Schrader, L. U., Brandt, L., and Henningson, D. S., "Receptivity mechanisms in three-dimensional boundary-layer flows," *Journal of Fluid Mechanics*, Vol. 618, 2009, pp. 209–241.

[28] Dagenhart, J. R., and Saric, W. S., "Crossflow stability and transition experiments in swept-wing flow," 1999.

[29] Raffel, M., Merz, C. B., Schwermer, T., and Richter, K., "Differential infrared thermography for boundary layer transition detection on pitching rotor blade models," *Experiments in Fluids*, Vol. 56, No. 2, 2015. https://doi.org/10.1007/s00348-015-1905-y.

[30] Wieneke, B., "PIV uncertainty quantification from correlation statistics," *Measurement Science and Technology*, Vol. 26, No. 7, 2015, p. 074002. https://doi.org/10.1088/0957-0233/26/7/074002.

[31] White, E., Saric, W., Gladden, R., and Gabet, P., "Stages of swept-wing transition," *39th Aerospace Sciences Meeting and Exhibit*, 2001, p. 271.

[32] Kurz, H. B. E., and Kloker, M. J., "Mechanisms of flow tripping by discrete roughness elements in a swept-wing boundary layer," *Journal of Fluid Mechanics*, Vol. 796, 2016, pp. 158–194. https://doi.org/10.1017/jfm.2016.240.